

Proof of Concept Coded Aperture Miniature Mass Spectrometer Using a Cycloidal Sector Mass Analyzer, a Carbon Nanotube (CNT) Field Emission Electron Ionization Source, and an Array Detector

Jason J. Amsden,¹ Philip J. Herr,¹ David M. W. Landry,¹ William Kim,¹ Raul Vyas,¹ Charles B. Parker,¹ Matthew P. Kirley,¹ Adam D. Keil,² Kristin H. Gilchrist,³ Erich J. Radauscher,¹ Stephen D. Hall,³ James B. Carlson,³ Nicholas Baldasaro,³ David Stokes,³ Shane T. Di Dona,¹ Zachary E. Russell,^{1,4} Sonia Grego,³ Steven J. Edwards,⁵ Roger P. Sperline,⁵ M. Bonner Denton,⁵ Brian R. Stoner,^{1,3} Michael E. Gehm,¹ Jeffrey T. Glass¹

¹Department of Electrical and Computer Engineering, Duke University, Durham, NC 27708, USA

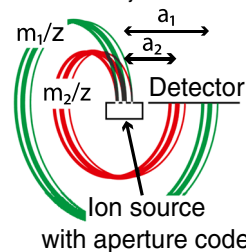
²Broadway Analytical, LLC, Monmouth, IL 61462, USA

³Engineering and Applied Physics Division, RTI International, Research Triangle Park, NC 27709, USA

⁴Present Address: Ion Innovations, Peachtree Corners, GA 30092, USA

⁵Department of Chemistry and Biochemistry, University of Arizona, Tucson, AZ 85721, USA

Coded Apertures and Cycloidal Mass Analyzers



Abstract. Despite many potential applications, miniature mass spectrometers have had limited adoption in the field due to the tradeoff between throughput and resolution that limits their performance relative to laboratory instruments. Recently, a solution to this tradeoff has been demonstrated by using spatially coded apertures in magnetic sector mass spectrometers, enabling throughput and signal-to-background improvements of greater than an order of magnitude with no loss of resolution. This paper describes a proof of concept demonstration of a cycloidal coded aperture miniature mass spectrometer (C-CAMMS) demonstrating use of spatially coded apertures in a cycloidal sector mass analyzer for the first time. C-CAMMS also incorporates a miniature carbon nanotube (CNT) field emission electron ionization source and a

capacitive transimpedance amplifier (CTIA) ion array detector. Results confirm the cycloidal mass analyzer's compatibility with aperture coding. A >10× increase in throughput was achieved without loss of resolution compared with a single slit instrument. Several areas where additional improvement can be realized are identified.

Keywords: Cycloidal mass analyzer, Coded apertures, Miniature mass spectrometer, Carbon nanotube, Ion array detector

Received: 28 April 2017/Revised: 11 September 2017/Accepted: 21 September 2017/Published Online: 19 October 2017

Jason J. Amsden and Philip J. Herr contributed equally to this work.

Electronic supplementary material The online version of this article (<https://doi.org/10.1007/s13361-017-1820-y>) contains supplementary material, which is available to authorized users.

Correspondence to: Jeffrey Glass; e-mail: jeff.glass@duke.edu

Introduction

Field able and miniature mass spectrometers (<20 kg and the size of a suitcase or less) [1] have many potential applications in environmental monitoring [2–5], explosives trace detection [6, 7], point of care medicine [8, 9], and space exploration [1]. There are several types of mass analyzers for miniature mass spectrometers, including ion trap, quadrupole, time-of-

flight, and sector analyzers [1]. However, miniaturization of mass spectrometers, and sector instruments in particular, leads to a throughput versus resolution tradeoff and poor performance relative to laboratory instruments, limiting their use in the field. Of the instruments mentioned above, a sector instrument has a slit at the exit of the ion source and at the collector that can be adjusted to set the instrument resolving power [10]. To maintain resolution when miniaturizing the instrument, the width of the slits must also shrink, thereby reducing instrument throughput and sensitivity. As a result, in a miniature sector instrument, one can either have high resolution and low throughput, or low resolution and high throughput, but not both high resolution and high throughput.

Recently, the application of coded apertures to sector mass spectrometers has eliminated the tradeoff between throughput and resolution in sector mass spectrometry [11]. By replacing the slit in a simple 90° magnetic sector with a 1-dimensional (1D) or 2-dimensional (2D) array of slits called a coded aperture, an increase in throughput of over an order of magnitude was achieved without loss in resolution [12, 13]. In addition, compatibility of aperture coding was demonstrated with the Mattauch-Herzog double focusing sector analyzer. However, imaging of the coded aperture pattern at the detector was relatively poor, due to the narrow electric sector and fringing fields [14]. To address this problem, the current work utilizes a cycloidal mass analyzer.

The cycloidal mass analyzer was introduced in 1938 by Walter Bleakney and John A. Hipple, Jr. at Princeton University, Palmer Physical Laboratory [15, 16]. The analyzer employs uniform, perpendicular electric and magnetic fields. In a uniform magnetic field, charged particles traverse circular trajectories. In a uniform electric field, charged particles exhibit linear motion. In perpendicularly oriented uniform electric and magnetic fields, a charged particle exhibits circular motion with translation, i.e., cycloidal trajectories. Solving the equations of motion for a charged particle in perpendicularly oriented uniform electric and magnetic fields yields an equation for the pitch, a_i

$$a_i = \frac{m_i}{z} \frac{2\pi E}{B^2} \quad (1.1)$$

or displacement of the ion from the ion source exit slit after it travels through 360°, where m_i is the mass of the i^{th} ion, z is the charge on the ion, E is the applied uniform electric field, and B is the applied uniform magnetic field (Figure 1a). This equation does not depend on the initial energy or angle of the ion as it exits the ion source. Therefore, unlike other double focusing sector analyzers, such as the Mattauch-Herzog and Bainbridge-Jordan that correct for initial energy and angular distributions of the ions to first order, the cycloidal mass analyzer perfectly corrects for the initial energy and angular distribution of the ions [16]. Furthermore, Figure 1b shows that the cycloidal mass analyzer is inherently compatible with aperture coding. In the figure, the red trajectories represent ions with mass to charge m_1/z and the green trajectories represent ions with mass

to charge m_2/z . Unlike the single slit in Figure 1a, the ion source has an aperture with multiple slits. Owing to the focusing properties of the cycloidal mass analyzer, a perfect image of the pattern of slits at the ion source is projected on the detector for each mass to charge ratio [11].

Despite their unique focusing properties, cycloidal mass analyzers have historically seen relatively few applications. In the late 1930s, Mariner and Bleakney developed a 262 mm focal length cycloidal instrument aimed at achieving a resolution of 25,000 [17]. In the 1940s, a group at Carbide and Carbon Chemical Corporation in Oak Ridge Tennessee developed a 40 cm focal length instrument for isotopic analysis [18, 19]. The 1950s and 1960s saw the first commercially produced cycloidal mass spectrometers. First, an instrument developed by Consolidated Electrodynamics Corporation for process gas analysis aimed to bring “mass spectrometry out of the laboratory...into the plant [20].” The team at Consolidated Electrodynamics Corporation also published papers investigating the effects of non-uniform fields [21] and space charge [22] in cycloidal focusing mass analyzers, as well as the design for a small general purpose cycloidal mass analyzer [23]. In the 1960s, Varian Analytical Instrument Division released the M-66 cycloidal mass spectrometer, which was advertised as a relatively small, inexpensive instrument with high performance (mass range to 2000 u and resolution ≥ 2000) [24–26]. Benz and Brown observed metastable ions using the Varian M-66 [27]. Also in the 1960s, a group from The Netherlands proposed a “virtual slit” cycloidal mass analyzer [28] with 100% collection efficiency and used it later in the 1980s to investigate the dissociative ionization of toxic gases [29]. The 1970s and 1980s saw the first multi-collector cycloidal mass analyzers designed to take advantage of the linear focal plane of the cycloidal mass analyzer. First, Adams and Smith employed a multichannel plate array with metal strip detectors placed behind the multichannel plate [30, 31]. In 1985, Halas S. published on a dual collector cycloidal mass analyzer for detection of hydrogen isotopes [32]. In 1991, Harry Hemond published a paper detailing the design of a backpack-portable cycloidal mass spectrometer based on the design used in the Consolidated Electrodynamics cycloidal mass analyzer [33]. This work led to the creation of the NERUS (novel, efficient, rapid evaluation of underwater spectra) instrument with Harry Hemond and Richard Camilli [34, 35] and eventual collaboration between Woods Hole Oceanographic Institute and Monitor Instruments, Inc. on the TETHYS (tethered yearlong spectrometer) instrument [4, 36] for continuous underwater monitoring. Recently, Southwest Research Institute developed a proof of concept multi-collector cycloidal mass analyzer with 7 Faraday cup collectors for isotope ratio measurements [37].

There are two main reasons cycloidal mass analyzers have had relatively few applications since their invention in 1938 [15]. First, as the ion source must be placed inside the magnetic field, the ion source must be small to keep the overall size of the instrument relatively small. The typical thermionic filament electron ionization source can be made small, but one must deal with the considerable heat generated by the thermionic

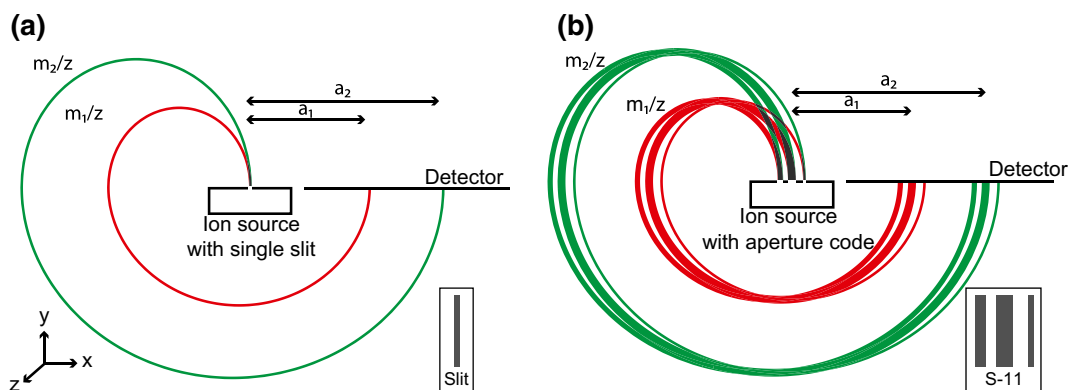


Figure 1. Cycloidal ion trajectories for two different mass to charge ratios, m_1/z (red trajectory) and m_2/z (green trajectory), where $m_2 > m_1$. In the figure, the electric field is in the negative y -direction and the magnetic field is in the negative z -direction: (a) a conventional single slit instrument and (b) a coded aperture instrument with an S-11 coded aperture. The width of the slit and width of the minimum feature size in the coded aperture are $50\ \mu\text{m}$. The S-11 consists of a $100\ \mu\text{m}$ slit, a $100\ \mu\text{m}$ separation, a $150\ \mu\text{m}$ slit, a $150\ \mu\text{m}$ separation, and a $50\ \mu\text{m}$ slit. See section below for more information on the coded aperture

filament. In addition, the thermionic filament requires substantial power, unfavorable in a portable instrument. Second, a key advantage of the cycloidal mass analyzer is the ability to focus different mass to charge ratios in a linear plane, allowing collection of an entire mass spectrum without scanning. To fully take advantage of this property, an array detector, similar to those used in optical spectroscopy, is required. Cycloidal mass analyzers require that the detector be placed in the magnetic field. Typical ion detector arrays, such as multichannel plate electron multipliers, do not work well in magnetic fields. Adams and Smith used a multichannel plate electron multiplier in a cycloidal instrument, however the instrument had limited dynamic range and sensitivity [30, 31]. Without a multichannel detector, the cycloid mass analyzer must be operated by scanning the electric and/or magnetic field and therefore does not have significant advantages over other scanning mass analyzers, such as the ion trap and quadrupole mass filter.

This paper describes a proof of concept cycloidal coded aperture miniature mass spectrometer (C-CAMMS). C-CAMMS consists of a miniature cycloidal mass analyzer with a miniature carbon nanotube (CNT) field emission electron ionization source, a novel permanent magnet geometry, and a 1704 channel high-sensitivity ion array detector that functions in a magnetic field. In addition, this instrument takes full advantage of the unique focusing properties of the cycloidal mass analyzer by applying aperture coding to increase the instrument throughput without changing the system resolution. The following sections describe the design of the C-CAMMS instrument and some preliminary results characterizing the performance of the instrument, focusing on the ability to image a coded aperture.

Mass Spectrometer Subsystem Design

C-CAMMS consists of a sample inlet, ion source, mass analyzer, detector, control electronics, and vacuum system. A block diagram and a photograph of the C-CAMMS system,

with the various components labeled, is shown in Figure S1 of the Supplementary Material. For this proof of concept demonstration, we focused our efforts on the development, miniaturization, and integration of the ion source, mass analyzer, and detector and did not optimize or miniaturize the inlet, vacuum system, or control electronics. Miniaturization and optimization of the inlet, vacuum system, and electronics will be addressed in later generation systems.

Ion Source

A typical electron ionization source contains a thermionic electron source. Thermionic sources have been well documented and produce stable electron current densities. However, thermionic electron sources have several disadvantages when used in miniature mass spectrometers, including high power consumption, short lifetimes, low current density, and the inability to be pulsed on and off frequently [38].

Field emission electron sources using carbon nanotubes (CNTs) have the potential to address the disadvantages of thermionic electron sources for miniature mass spectrometry applications [39, 40]. CNTs require no heating for electron emission, significantly reducing the amount of power consumed during operation. Lifetimes of CNTs during continuous use exceed 500 hours and the ability to be pulsed on and off many thousands of times has also been demonstrated [39]. Several groups have developed field emission cathodes for miniature ion sources, including an electron ionization source and chemical ionization sources for portable mass spectrometers [39–44].

Our group has developed a micro electromechanical systems (MEMS) vacuum microelectronic device platform with CNT field emitters for many applications [45, 46]. Recently, Radauscher et al, reported a miniature electron ionization source designed for a cycloidal mass analyzer using a MEMS device with integrated CNT field emission cathodes and a low-temperature co-fired ceramic (LTCC) scaffold [47]. This ion source had an ion energy distribution of $22 \pm 6\ \text{eV}$, with an

angular distribution of $0 \pm 6.5^\circ$ at the midplane (the plane parallel to the electric field and perpendicular to the magnetic field of a cycloidal mass analyzer that exhibits double focusing) and $0 \pm 5^\circ$ out of plane (the plane parallel to the electric field and parallel to the magnetic field). Large angular dispersion out of plane is a significant disadvantage in a cycloidal mass analyzer. The focusing properties of the cycloidal mass analyzer compensate for the angular dispersion in the midplane. However, velocity components that are out of plane result in the ions being focused in a line rather than a point at the detector [28]. As the path length of the ions becomes longer for those ions with larger mass to charge ratio, the focus line will increase in length and lead to a reduction in signal intensity when the focus line becomes longer than the detector elements.

The ion source in the C-CAMMS is similar to the miniature Neir-type electron ionization source described in reference [47], which was fabricated using microelectromechanical systems (MEMS) with integrated CNT field emission cathodes and a low-temperature co-fired ceramics (LTCC) scaffold. In the C-CAMMS ion source, the MEMS device described in [47] is replaced with a CNT-coated silicon chip and an electroformed metal box for the ionization volume. A section in this manuscript and Figures S1–S4 of the Supplementary Material detail the design and fabrication of the ion source. As shown in the Results section, the changes enabled reduction in the angular dispersion in the plane perpendicular to the cycloidal trajectories where the cycloid does not provide double focusing.

For the mass spectra shown in the Results section, we used two different apertures, including a single 50 μm slit and a cyclic S code [48] of order 11, or S-11, coded aperture consisting of three slits of widths 150, 100, and 50 μm (Figure 1b). The minimum feature size of the single slit and S-11 coded aperture are the same to allow comparison of throughput and resolution in the reconstructed spectra with that of the single slit. The S-11 coded aperture provides $6\times$ the throughput of the single slit, as it has $6\times$ the open area. The typical operating parameters for the ion source include an electron emission current of 200–500 nA, between -160 V and -200 V on the CNT cathode (yielding ~ 200 – 240 eV electrons for ionization), 40 V on the ionization volume, 17 V on the extraction aperture, and 0 V on the coded aperture.

Cycloidal Mass Analyzer

The mass analyzer consists of a magnet, electric sector, and vacuum manifold. Figure 2a shows a CAD drawing and Figure 2b shows a photograph of the mass analyzer, including the ion source and detector, with the various components labeled. The overall dimensions of the mass analyzer are 207 mm \times 130 mm \times 100 mm with an approximate weight of 10 kg. The magnet is composed of two Nd-Fe-B bar magnets and two high permeability stainless steel plates to complete the magnetic circuit and results in a uniform field of 0.3 T directed along the x-axis in the gap. Further details on the magnet design

and how field uniformity affects aperture imaging are described in Landry et al. [49].

To create a uniform electric field in the $-y$ -direction, we use the fact that the electric field is the negative gradient of the electric potential. In this case, solving the differential equation yields

$$V = -Ey \quad (2.1)$$

where V is the electric potential, E is the desired electric field, and y is the y -coordinate. To generate the desired electric field, we created an electric sector comprising an array of 25 electrodes separated by 0.5 mm. The array was oriented parallel to the y -axis, forming an L-shaped box 91 mm \times 78 mm \times 14 mm with the ion source positioned in the center. All electrodes are 3 mm wide, except for the top and bottom electrodes, which are 1.5 mm wide and electrically connected to caps on the box. The potential on each electrode is set by the equation

$$V_i = \left(\frac{i-13}{13}\right)Ed \quad (2.2)$$

where V_i represents the voltage on the i^{th} electrode, where $I=1$ for the bottom electrode in Figure 2a; d is the distance between the top and bottom electrodes, $\left(\frac{i-13}{13}\right)d$ corresponds to the y -coordinate in Equation (2.2); and E is the desired electric field magnitude. This arrangement of potentials was chosen such that the center electrode, aligned with the top of the ion source and detector, is at 0 V. To construct the electric sector, FR4 PC board material is fabricated with gold 3 mm wide traces/0.5mm spaces on the inner surfaces to make the electrodes. On the outer surface of the PC board, a series of 1 M Ω resistors are arranged in a voltage divider circuit. Further details on the electric sector, including evaluation of field uniformity and its effects on aperture imaging, are described by Landry et al. [49]. The electric sector used here is the Configuration 1 described in that paper.

The vacuum manifold is a block of 6061 aluminum machined into a hollow I-beam shape. The electric sector and detector are attached to a PC board that seals the vacuum chamber and provides vias for electrical connections to components inside the vacuum manifold. Figure 2b shows a photo of the PC board with the detector, ion source, and electric sector partially inserted into the vacuum manifold. The opposite side of the vacuum manifold from the PC board feedthrough contains a hole that allows connection to standard KF-25 vacuum fittings.

Detector

The array detector used here is similar to the 4th generation 1696 channel capacitive transimpedance amplifier (CTIA) array described previously [50]. The 8th generation detector used here incorporates three significant improvements. First, it has a 100% fill factor. The 100% fill factor is accomplished by making overlapping metal detector fingers in two metal layers of the CMOS process used to fabricate the detector. Using a via

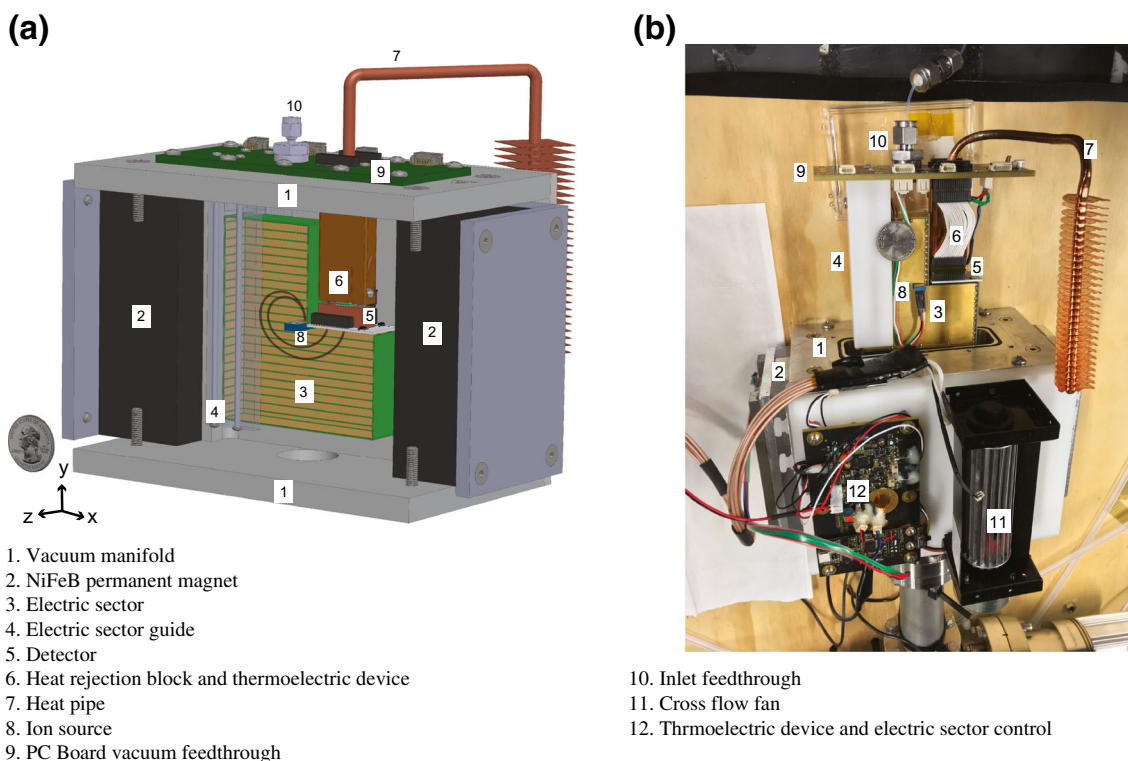


Figure 2. (a) CAD model of the cycloidal mass analyzer. In the figure, the high permeability stainless steel plates, part of the vacuum manifold, and one side of the electric sector are invisible to show the detail inside the magnet and vacuum manifold. Example cycloidal ion trajectories are shown in grey. (b) Photograph of the cycloidal mass analyzer with electric sector removed from the magnet and vacuum manifold. A quarter is included in each image for scale

to connect overlapping fingers in each layer enables the 100% fill factor. As such, the 8th generation detector is 21.3 mm wide with 1704 12.5 μm wide, 3 mm tall detector fingers. Second, it incorporates four gain stages in the amplifier, including an ultra-high gain stage that uses a 4 f. capacitor. All data in this paper were taken using the gain stage with the 4 f. capacitor. Finally, it incorporates a significantly smaller ceramic chip carrier than earlier generations, which enables a smaller gap between the poles of the magnet.

To reduce thermal noise in the detector, we designed a thermal management system that includes a copper heat rejection block, a copper heat pipe, and a thermoelectric device. The thermoelectric is $6.6 \times 6.6 \times 1.5$ mm (Custom Thermoelectric, Bishopville, MD, USA, Model number 03101-9B30-30RU7). It has a maximum ΔT spec of 69 K ($Q = 0$ W) with a Q_{max} of 6.75 W ($\Delta T = 0$ K). The device was selected to support pumping approximately 1 W of heat with a ΔT of 40 K to achieve a detector temperature of approximately -5 °C. The thermoelectric is sandwiched between a small copper block attached to the detector ceramic carrier detector and the larger copper heat rejection block. A 5 mm outer diameter copper heat pipe conducts heat from the copper heat rejection block in the vacuum chamber to an array of 31 fins that are cooled externally with a cross-flow blower (EBM-PAPST Inc, Farmington, CT, USA). The heat pipe is approximately 45 cm long, with an array of fins covering the last 11 cm. The pipe provides a flexible approach for removing the heat from the detector

cooling block and arranging the integrated system (see Figure 2a and b). Using this setup, we are able to reduce the detector temperature to approximately -5 °C.

Inlet and Vacuum System

The inlet for C-CAMMS is a 1/16 inch diameter Teflon tube that passes through the vacuum manifold through a Swagelock fitting. This tubing is connected to a needle valve that can control the flow of gas into the system. The needle valve is connected to a gas mixing system consisting of several mass flow controllers and pressurized gas cylinders. For the data collection shown below, we used a flow of 100 sccm of Ar and 100 sccm of dry air and mixed the gas in 40 feet of 1/4 inch diameter tubing. After flowing for 20 min to ensure adequate mixing, we used the needle valve to allow a small amount of the mixed gas into the mass analyzer through the 1/16 inch tubing.

The vacuum system includes an Agilent Technologies IDP-15 Dry Scroll vacuum pump backing a Agilent Turbo V81M turbo pump. As mentioned above, for the proof of concept system, we did not attempt to miniaturize the vacuum system. A future manuscript will include a portable vacuum system currently under development. The system base pressure is 2×10^{-6} Torr. Data collection occurs at approximately 5×10^{-5} Torr. The mass analyzer is connected to the vacuum system with a stainless steel cross (Supplementary Figure S1b).

Control System

The system is controlled by a combination of custom circuits and software packages and Keithley Instruments source meters. Potentials for the ion source, extraction, grid, and source voltages are provided by three Keithley 2410 source measure units controlled by LabView software. A custom control system provides a basic framework for the required custom circuits and a USB-connected user interface for manipulation of the circuits for correct operation. The control system operates and derives the required independent voltages from a single 24 V DC power supply. The 24 V DC selection provides a single common voltage for all parts of the system, both current and future, to operate.

Using a JAVA application connected through a USB interface, the control system provides control of a buck converter using pulse width modulation (PWM) to drive the thermoelectric device. User options allow the PWM driving the thermoelectric device to be set from 0% to 90%. A platinum resistance temperature device measures the detector temperature. The electric sector voltages are generated from independent buck-boost circuits and can be set with the user interface over ± 10 –50 V. The required +6-volts and +13-volts power for the detector is derived using buck converters. A separate USB interface and Python application control the detector. The power requirement for the detector (including thermal management) and electric sector is approximately 31 W.

Mass Range and Resolving Power of C-CAMMS

The mass range and resolving power of C-CAMMS depends on the electric and magnetic field magnitudes and the width and position of the detector. From Equation (1.1) for the pitch of a cycloidal mass analyzer (distance between the ion source and position of focus of a particular m/z ratio on the detector plane), it is evident that the change in mass between opposite ends of the detector is given by the following equation:

$$L = \frac{B^2 dz}{2\pi E} \quad (2.3)$$

where L is the difference in mass between opposite ends of the detector, B is the magnetic field strength, d is the width of the detector, E is the electric field strength, and z is the ion charge. The resolving power, R is equivalent to the width of the smallest slit in the aperture, s divided by the distance between adjacent masses, x . The distance between adjacent masses is the width of the detector, d divided by the change in mass between opposite ends of the detector, L . Using the definition of resolving power and Equation (2.3), the resolving power of a cycloidal mass analyzer is:

$$R = \frac{sL}{d} = \frac{szB^2}{2\pi E} \quad (2.4)$$

Solving Equation (2.4) for the electric field E , and inserting into Equation (1.1) yields an alternative equation

for the pitch a , in terms of the resolving power and slit feature size:

$$a = \frac{ms}{R} \quad (2.5)$$

Figure 3 shows plots of a versus m for a 50 μm slit and various resolving powers. In the figure, the shaded grey area represents the extents of the detector relative to the ion source in C-CAMMS and indicates the mass range in atomic mass units for the various resolving powers. C-CAMMS has a magnetic field of 0.3 T. Therefore, each mass range and resolving power in Figure 3 is accessible by adjusting the electric field from Equation (2.4).

For the data in the Results section, we chose to use an electric field of 823 V/m giving an expected resolving power of ~ 0.08 u with a mass range of $m/z = 11$ –45 u, a S-11 coded aperture with a 50 μm minimum feature size, and a mixture of 50% Ar and 50% dry air. A mixture of Ar and air was chosen as it has mass to charge peaks distributed relatively evenly throughout the mass range and for the coded aperture spectra, none of the aperture images will overlap, facilitating evaluation of the aperture imaging quality.

Results

Ion Source Characterization

Ion Source Simulation The goal for the ion source is to produce an ion beam with an energy between 15 and 20 eV and minimal energy and angular dispersion. This section

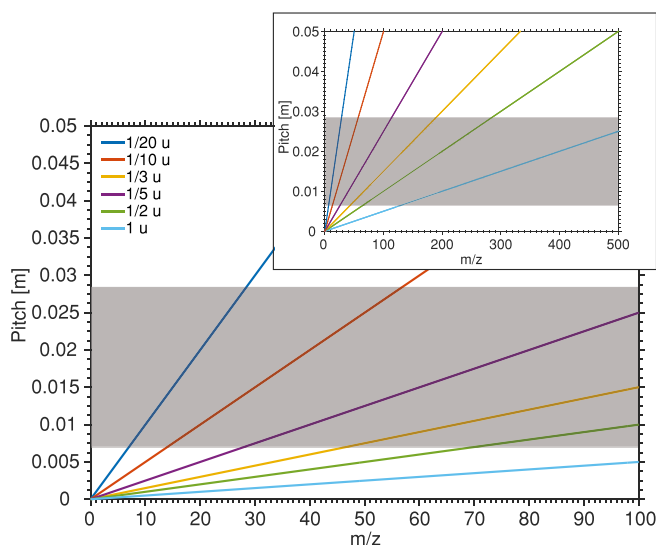


Figure 3. Plot of cycloidal mass analyzer pitch (distance between ion source and position of focus for a particular m/z ratio on the detector plane) versus mass to charge ratio for various resolving powers. The grey box represents the position and extent of the detector relative to the ion source at position (0,0) for the C-CAMMS system showing the mass ranges and resolving powers achievable. The inset displays the same data, but for a larger range of masses

presents a simulation model of the ion source using the electron and ion optics program SIMION 8.1. The goal of the simulations was to improve upon the performance of the MEMS-based ion source described previously [47] by optimizing the operating voltages of the ion source presented in a Section above.

In SIMION, geometry files are written to describe the dimensions and structure of the ion source, and voltages are specified for each component. SIMION numerically determines the potential landscape of the structure, creating a potential array file that is used to simulate electron and ion trajectories within the geometric model. We simulated the CNT cathodes with the ionization box, extraction aperture, and spatial filter to determine the trajectories and energies of the ions that were exiting the ion source model. This information allowed us to calculate the energy and angular dispersion of the ions. In our simulations, we assumed uniform electron field emission from the CNTs and that electrons entering the ionization volume create ions randomly along their path inside the volume. Each ion source geometry and potential configuration was simulated with up to 10,000 electrons and ions per simulation. We used an iterative process to quickly converge on a set of parameters with exit ion energies, energy dispersion, and angular dispersion that met our goals.

Figure 4a shows a 3D SIMION model of the ion source. Electron trajectories are shown in black and ion trajectories for

singly charged ions of mass 40 u are shown in red. There is a 0.08 T magnetic field in the simulation, matching the experimental setup for measuring the energy and angular dispersion, described below. Simulations indicate that to produce an ion energy of 18 ± 2 eV, the electrode potentials should be as follows: ionization box at 20 V, the extraction aperture at 6.5 V, and the spatial filter at 0 V. If different ion energies are needed for the mass analyzer, the potentials can be changed. The potential on the cathode was chosen as -120 V to match the potential difference between the cathode and ionization volume needed for field emission from the CNTs. Figure 4b and c show the equipotential lines and ion trajectories along cut planes through the center of the ion source. The XY-plane in our simulation is the plane where the cycloid does not correct for angular dispersion (Figure 4b). The YZ-plane is the plane where the cycloid exhibits perfect double focusing (Figure 4c). The blue equipotential lines are 2 V apart and labeled in each plane. Electron trajectories are black and ion trajectories are red. The angular spread of ions leaving the ion source in the XY-plane is $0 \pm 1^\circ$. The ionization volume structure and dimensions in the XY-plane provides the equipotential landscape needed for low angular dispersion. The ions travel perpendicular to the apertures because the equipotential lines and bottom substrate are parallel to the apertures. The extraction aperture is a single $1 \text{ mm} \times 1 \text{ mm}$ opening that blocks ions

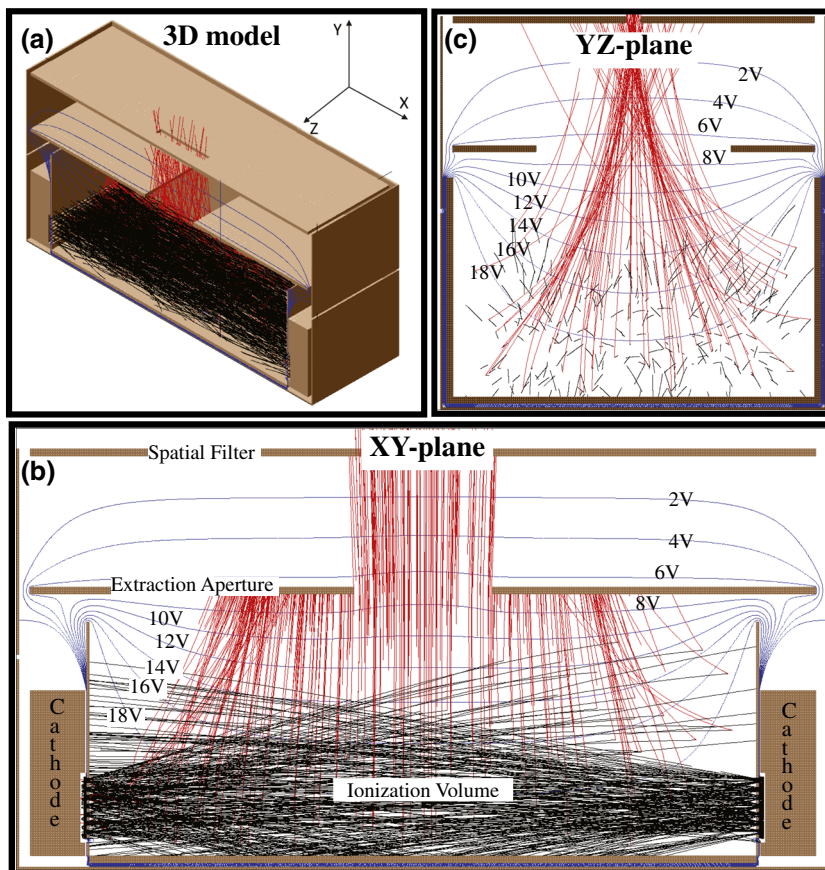


Figure 4. Results from ion source SIMION simulation. Ion trajectories are colored red, electron trajectories are black, and 2V spaced equipotential lines are blue. (a) 3D model of the ion source. (b) 2D cross-section in the YZ-plane passing through the center of the ionization box. (c) 2D cross-section in the XY-plane passing through the center of the ionization box

formed near the boundary of the ionization volume where the equipotential lines are curved. In the YZ-plane, the calculated value of angular spread is $0 \pm 4^\circ$. This value of angular dispersion could be lowered by widening the ionization box to flatten the equipotential lines. However, this would increase the size of the ion source by a few mm, so we chose to keep the dimensions of the ion source small and let the cycloidal mass analyzer correct the dispersion in this dimension.

Ion Source Experimental Measurements

To characterize the ion source, we performed measurements of the energy and angular dispersion and then compared to the simulation results.

Energy Dispersion The energy dispersion of the ion source was characterized using a stopping potential experiment. In this experiment, the ion source and the CTIA detector described above were aligned so that ions exiting the ion source will collide with the detector's surface. A metal retarding grid is placed between the ion source and detector and its potential varied. Ions created in the ion source travel out of the spatial filter through a cylindrical cavity towards the retarding grid. If an ion has a kinetic energy in electron volts that is greater than the potential placed on the retarding grid, the ion will pass through the grid and collide with the CTIA detector. During the experiments, the detector is cooled to -5°C by a thermoelectric device to reduce thermal noise. All components are mounted to a PC board that serves as the vacuum feedthrough. The system pressure is held at 5×10^{-5} Torr by controlling the flow through the needle valve. The vacuum chamber is an aluminum block and two permanent magnets (K&J Magnetics B88X0 Ni-Fe-B) are located on opposite sides of the aluminum block to create a

0.08 T magnetic field parallel to the electron trajectories. Figure 5a provides a schematic of the experimental measurement device. Photographs of the experimental setup have been presented elsewhere [47].

Using Keithley 2410 source measure units, the ion source components were initially biased with the values determined by the simulations in section above (ionization volume at 20 V, extraction aperture at 6.5 V, and the spatial filter at 0 V). The potential on the cathode was varied from -160 V to -140 V to achieve a constant $1 \mu\text{A}$ of electron emission. However, as was observed in the MEMS based ion source reported previously, the potentials predicted by simulation did not result in an ion signal at the detector. As a result, we placed the ion source in the C-CAMMS first generation prototype and determined the voltages that produced the best mass spectrum. These voltages were 40 V on the ionization box, 17 V on the extraction aperture, and 0 V on the spatial filter. The difference in the voltages predicted by simulation and those producing the best spectrum are discussed below.

Using the voltages determined using the C-CAMMS prototype, the energy dispersion was measured by scanning the voltage applied to the retarding grid from 0–30 V in 1 V steps. At each voltage step, the detected ion current data was recorded 50 times. Any data point two standard deviations from the mean was removed. This was done to account for the ion signal fluctuations caused by tracking error in the constant current circuit. To produce a constant current from a CNT bundle, a varying cathode voltage was produced by the Keithley 2410. When the voltage needed to provide a constant current changes faster than the Keithley 2410 can adjust for, it overcorrects the voltage, therefore the ion current fluctuations follow the fluctuation in cathode voltage. After correcting for these fluctuations, measuring the full width at half maximum (FWHM) of the derivative of the stopping potential curve yielded an energy dispersion of 14 ± 2 eV (Figure 5b).

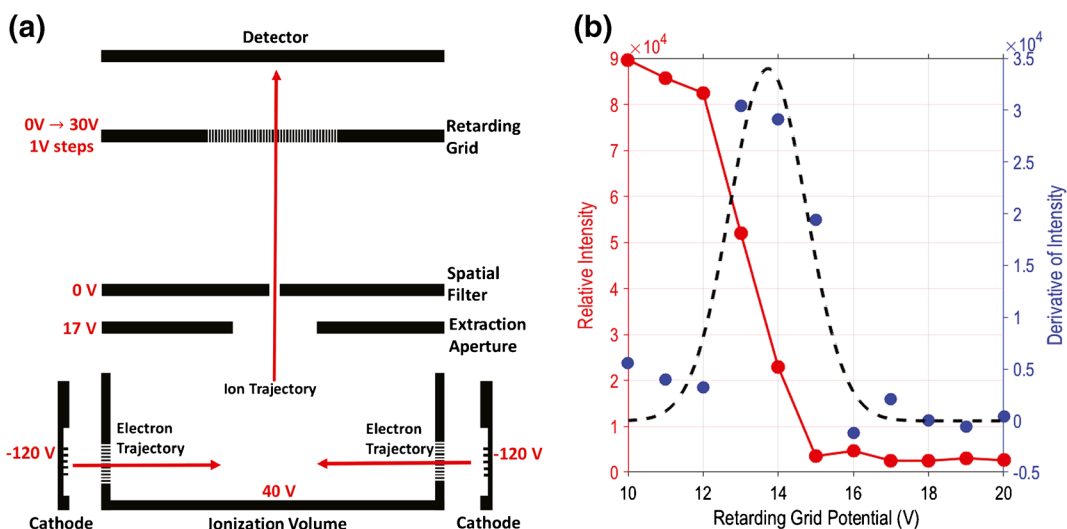


Figure 5. (a) Schematic of energy dispersion experimental setup. (b) Energy dispersion data. Ion current intensity is shown on the left y-axis, sweeping retarding grid potential on the x-axis, the derivative of the retarding potential data on the right y-axis, and the fitted Gaussian as the dashed black line. The average energy of the ions was 14 eV with a FWHM energy dispersion of 2 eV

Angular Dispersion Angular dispersion along two planes was measured using the setup described in reference [47] with the same potentials used to measure energy dispersion. The angular dispersion along the mass dispersive plane, corresponding to the YZ-plane in the simulation, was calculated by comparing the spatial filters width to the width of the ion signal's extent on the detector and measuring the distance between the ion source and detector. The measured angular dispersion was $0 \pm 9^\circ$, approximately $2\times$ the simulated value. The angular dispersion in the out-of-plane direction, corresponding to the XY-plane in simulation, was evaluated inside the cycloidal mass analyzer and described in another section.

Difference Between Ion Source Simulation and Experiment

Similar to the MEMS-based CNT field emission ion source described previously, the potentials suggested by simulation did not produce a signal at the detector. Achieving a signal required increasing the potentials [47]. Simulations using the voltages on the ion source electrodes optimized experimentally using C-CAMMS showed an energy of 37 ± 2 eV, about double the experimentally measured value. The angular spread in the XY-plane was $0 \pm 1^\circ$, and the angular spread in the YZ-plane was $0 \pm 4^\circ$, similar to the angular dispersion for the voltages optimized in simulation and half the experimentally observed value. Figure S5a and S5b show the equipotential lines, electron trajectories, and ion trajectories along cut planes through the center of the ion source for the voltages suggested by C-CAMMS optimization. The larger potentials required in the experiment could be a result of voltage drops due to contact resistances throughout the device. It is also possible that the simple field emission model assuming uniform emission from the surface of the CNT bundle is not correctly representing the electron trajectories from the CNTs through the grid and ionization volume. A difference in electron trajectories from the CNTs could change the ionization location resulting in a shift in the operating voltages required for ion detection. In addition, the simulation does not take into account space charge effects inside the ion source, which could affect the angular dispersion and explain the $2\times$ larger angular dispersion in the experimental measurement.

Results Using a Single 50 μm Slit

Figure 6a shows a comparison of experimental and simulated spectra of a mixture of 50% argon and 50% dry air using a single 50 μm slit at the exit of the ion source. The simulated spectrum is based on data from the NIST Chemistry WebBook [51] and assumes perfect mapping of the 50 μm slit to a 50 μm wide image at the detector. The spectra are normalized to the $m/z = 40$ peak. The peaks at $m/z = 20$ and 40 represent singly and doubly charged argon, respectively; $m/z = 14$ and 28 represent singly and doubly charged nitrogen, respectively; and $m/z = 16$ and 32 represent singly and doubly charged oxygen. The peaks are similar in relative intensity to the NIST data. This indicates that the angular dispersion of the ion source

in the YZ-plane where the cycloid does not have focusing properties is relatively small. If the energy dispersion were large in the YZ plane, the image of the slit would be magnified in the Z-direction as a function of the ion path length. Correspondingly, the intensity of the higher mass to charge ratios would be low due to ions hitting the detector plane outside the detector pixel active area. The spectrum also contains peaks at $m/z = 17$ and 18 indicating a small quantity of water in the system despite the use of dry air.

The resolving power of the experimental data, measured by taking the full width at half max of the peaks, ranges between 0.2 and 0.4 u, with better resolving power at lower m/z . In a perfect focusing cycloidal mass analyzer, the width of the peak on the detector should be the same as the width of the slit in the aperture over the entire mass range. In this case, the width of the slit is 50 μm , which corresponds to an expected resolving power of 0.08 u. There are several possibilities for the larger image of the slit at the detector, including uniformity of the electric field, alignment of the detector with the mass analyzer focal plane, and space charge. These possibilities are presented in more detail in the Discussion section.

To demonstrate the analysis of additional chemical species, spectra of lab air and methanol were also collected using both the C-CAMMS instrument and a Stanford Research Systems RGBA-300 (Figure S6).

Results with an S-11 Coded Aperture

Figure 6b shows a comparison of experimental and simulated spectra of a mixture of 50% argon and 50% dry air using a S-11 coded aperture with a 50 μm minimum feature size at the exit of the ion source. The S-11 aperture has an ideal throughput increase of $6\times$ over a single slit with the same minimum feature size. The simulated spectrum is based on data from the NIST Chemistry WebBook [51] and assumes perfect mapping of the S-11 aperture on the detector. The relative intensity is scaled such that the intensity of the peak corresponding to the 50 μm slit in the S-11 aperture at $m/z = 40$ has a relative intensity of 1. This will enable comparison of the relative intensity after reconstruction. The relative intensity of the aperture images for each mass-to-charge ratio match the NIST data very well. In addition, each of the three slits in the S-11 aperture are imaged for all mass-to-charge ratios. Figure 6c shows a magnified view of the aperture image for nitrogen at $m/z = 28$. The imaging is not ideal in that the signal does not go back to the baseline between the slits as it does in the ideal image. Similar to the single slit, the differences between the ideal and experimental data can be explained by the non-uniformity of the electric field, alignment of the detector with the mass analyzer focal plane, and space charge. These differences are presented in more detail in the Discussion section. In addition, the baseline near $m/z = 28$ and $m/z = 40$ shows some distortion between $m/z = 22-30$ and $m/z = 32-42$. A similar distortion is seen in the data from the 50 μm slit. This distortion may be due to ions with very large energy or oblique angles of exit from the ion source that result in scattering from the electric sector electrodes.

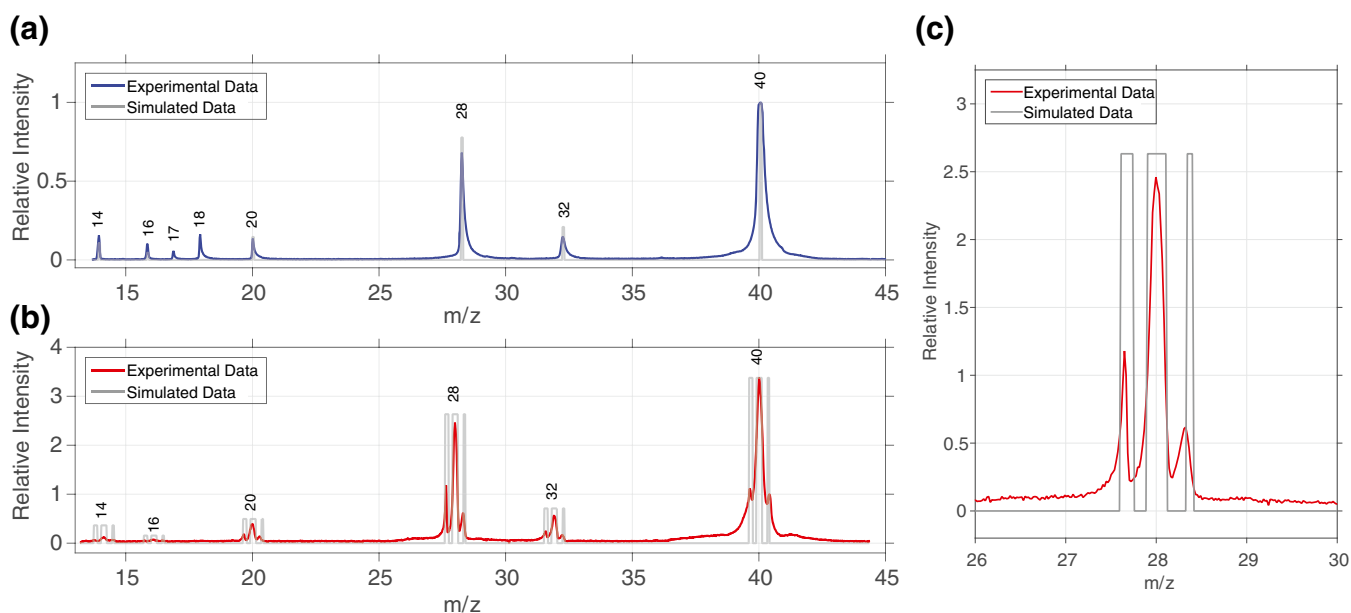


Figure 6. (a) Mass spectrum of a mix of 50% argon and 50% dry air using a 50 μm slit. The blue trace represents the experimental data and the gray histogram represents an ideal system based on the data from the NIST Chemistry WebBook. (b) Coded mass spectrum of a mix of 50% argon and 50% dry air using a 50 μm slit. The red trace represents the experimental data and the grey histogram represents an ideal system based on the data from the NIST Chemistry WebBook [51]. (c) Expanded view of the coded aperture image for $m/z = 28$

Spectral Reconstructions

In our previous work with the 90° sector, a sophisticated calibration process was required to reconstruct the spectra from the raw data as the 90° sector did not have the focusing properties of the cycloidal instrument [12, 13]. Here, since the cycloidal mass analyzer nominally produces a 1:1 image of the coded aperture on the detector, we can use a simple calibration and spectral reconstruction process.

The experimental measurement is the convolution of the system response with the input spectrum where m is the experimental measurement, s is the input spectrum, and r is the system response.

$$m = r * s \quad (3.1)$$

We can estimate the system response \hat{r} (note that variables with a caret represent estimations where variables without the caret are the true values), or calibrate the system by deconvolving the true spectrum s from the acquired measurements m

$$\hat{r} = [F[m]/F[s]] \quad (3.2)$$

where the “ F ” represents a Fourier transform operation, and “ F^{-1} ” represents an inverse Fourier transform operation. The system response r is analogous to the point spread function in optical imaging. Spectral reconstruction is then performed by de-convolving the acquired measurements m with the estimated system response \hat{r} , as follows:

$$\hat{s} = F^{-1}[F[m]/F[\hat{r}]]. \quad (3.3)$$

In practice, to de-convolve the acquired measurements with the system response we use the Richardson-Lucy de-

convolution algorithm as it is numerically more stable than the inverse Fourier transform [52, 53].

Figure 7a shows the results of a spectral reconstruction of the slit data compared with the raw data from the slit. The reconstructed data removes some of the peak broadening and has a better resolving power (~ 0.1 u FWHM) than the raw slit data, leading to an approximately 2.5 \times increase in signal intensity. Figure 7b shows the results of a reconstruction of the S-11 coded aperture compared with the results of the slit reconstruction. Here the results show an approximately 10 \times increase in signal intensity over the raw slit data. Furthermore, the resolving power is the same as that of the reconstructed slit data at 0.1 u (FWHM). However, the reconstruction is not perfect in that the peaks in the spectrum have small artifacts to the left of the main peak. These artifacts are likely a result of the imperfections in the imaging of the coded aperture due to the electric field uniformity and alignment of the mass analyzer focal plane with the detector as mentioned above and discussed below.

Discussion

The Results section shows the first application of coded apertures in a cycloidal mass analyzer. Results show that the cycloid is compatible with aperture coding. We achieved a >10 \times increase in instrument throughput with the S-11 coded aperture. However, the reconstructions showed some artifacts. We discuss below the three main factors affecting imaging quality in this first generation C-CAMMS prototype: field uniformity, position of the detector in the mass analyzer focal plane, and space charge.

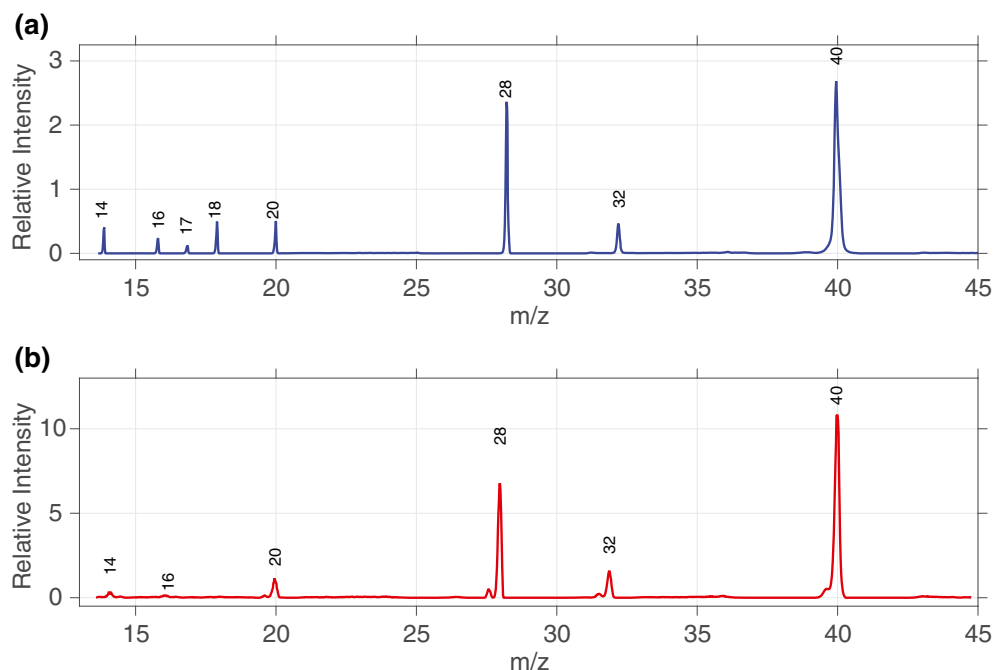


Figure 7. (a) Reconstructed data from the 50 μm slit. (b) Reconstructed data from the S-11 coded aperture

The imaging properties of the cycloidal mass analyzer depend on the uniformity of the electric and magnetic fields. Landry et al. [49] investigated using simulation the effects of field uniformity on the aperture imaging quality. Based on the simulation results, the magnet geometry used in C-CAMMS should have sufficient magnetic field uniformity to achieve good aperture imaging across the detector. However, the electric field produced by the electric sector configuration used here is not sufficient to achieve good aperture imaging due to non-uniform fields near the ion source. Landry et al. describe a new electric sector configuration that will correct this issue [49].

In addition to field uniformity, positioning the detector at the exact focal plane of the mass analyzer is required for optimal aperture imaging. Figure 8a and b show simulations of ion trajectories in a cycloidal analyzer with different initial energy and angular distributions using an S-11 aperture at the ion source. The insets show a magnified view of the trajectories as they cross the detector plane. For the simulation with ions that have a small initial momentum distribution, the depth of focus (DoF) is large, and the aperture is imaged on the detector over a wide range of positions (Figure 8a). However, for the simulation with ions that have a large initial energy and angular

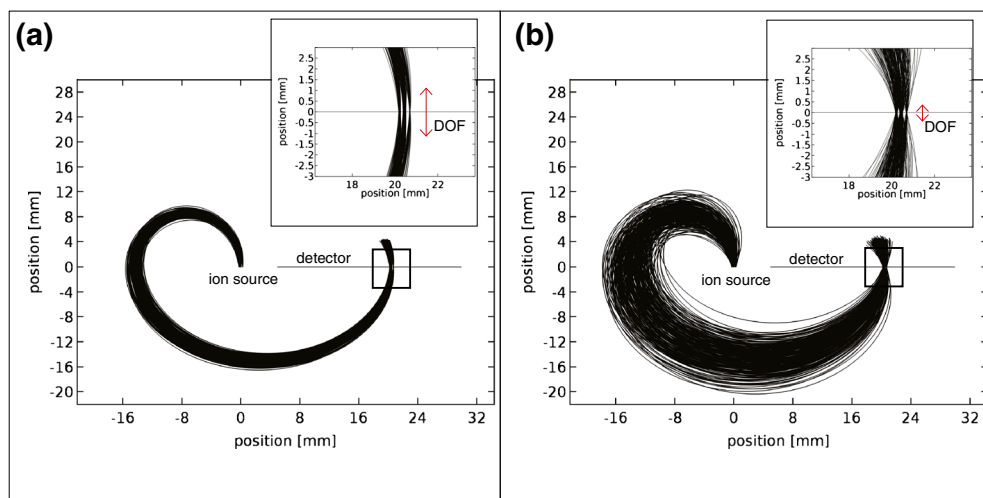


Figure 8. Comparison of the depth of field for aperture imaging for different energy and angular dispersions. (a) In this simulation, the ion source has an energy of 14.0 ± 0.5 eV and an angle of 0 ± 1 degrees. The inset shows that the depth of focus (DoF) is almost 3 mm. (b) In this simulation, the ion source has an energy of 14 ± 2 eV and an angle of 0 ± 8 degrees. The inset shows that the DoF for aperture imaging is less than 1 mm

distribution (close to the velocity distribution of the ion source used in the experiments), the DoF is small and the aperture is only imaged for a small range of detector positions (Figure 8b). Therefore, while the cycloid has perfect double focusing properties, the DoF for imaging is inversely proportional to the amount of dispersion in the ion source. In the current prototype, we have limited ability to change the position of the detector relative to the electric sector. Therefore, some of the blurring of the aperture image, as well as non-uniform resolving power across the detector, is a result of misalignment of the detector with the mass analyzer focal plane.

Space charge could also contribute to poor coded aperture imaging quality. Robinson showed that to first order, space charge effects shift the focal plane of the cycloidal mass analyzer [22]. As such, the effects of space charge will be similar to those described above for misalignment of the detector with the focal plane of the mass analyzer. Potential solutions to space charge and misalignment of the detector with the mass analyzer focal plane include addition of a linear positioner to adjust the relative position of the electric sector and detector plane or introduction of a linear gradient in the electric field, as suggested in Robinson et al. [21, 22].

Conclusion

This paper presented a proof of concept demonstration of a miniature cycloidal mass analyzer incorporating aperture coding, a CNT field emission electron ionization source, and an ion array detector. To improve coded aperture imaging, future prototypes will incorporate an improved electric sector with a more uniform field, similar to that described by Landry et al. [49], along with a linear positioner to adjust the position of the mass analyzer relative to the detector. In addition, as discussed above, there are several ways to improve the ion energy and angular dispersion and thereby increase the DoF. Finally, we will incorporate more complex coded apertures to further increase the instrument throughput as well as miniaturize the electronics and vacuum systems.

Acknowledgments

The information, data, or work presented herein was funded in part by the Advanced Research Projects Agency-Energy (ARPA-E), US Department of Energy, under Award Number DE-AR0000546. The views and opinions of authors expressed herein do not necessarily state or reflect those of the United States Government or any agency thereof.

References

1. Snyder, D.T., Pulliam, C.J., Ouyang, Z., Cooks, R.G.: Miniature and fieldable mass spectrometers: Recent advances. *Anal. Chem.* **88**, 2–29 (2016)
2. Mach, P.M., Winfield, J.L., Aguilar, R.A., Wright, K.C., Verbeck, G.F.: A portable mass spectrometer study targeting anthropogenic

- contaminants in sub-Antarctic Puerto Williams, Chile. *Int. J. Mass Spectrom.* (2016). <https://doi.org/10.1016/j.ijms.2016.12.008>
3. Bell, R.J., Davey, N.G., Martinsen, M., Collin-Hansen, C., Krogh, E.T., Gill, C.G.: A field-portable membrane introduction mass spectrometer for real-time quantitation and spatial mapping of atmospheric and aqueous contaminants. *J. Am. Soc. Mass Spectrom.* **26**, 212–223 (2015)
4. Camilli, R., Reddy, C.M., Yoerger, D.R., Van Mooy, B.A.S., Jakuba, M.V., Kinsey, J.C., McIntyre, C.P., Sylva, S.P., Maloney, J.V.: Tracking hydrocarbon plume transport and biodegradation at Deepwater Horizon. *Science*. **330**, 201–204 (2010)
5. Keil, A., Hernandez-Soto, H., Noll, R.J., Fico, M., Gao, L., Ouyang, Z., Cooks, R.G.: Monitoring of toxic compounds in air using a handheld rectilinear ion trap mass spectrometer. *Anal. Chem.* **80**, 734–741 (2008)
6. Sanders, N.L., Kothari, S., Huang, G., Salazar, G., Cooks, R.G.: Detection of explosives as negative ions directly from surfaces using a miniature mass spectrometer. *Anal. Chem.* **82**, 5313–5316 (2010)
7. Chen, C.-H., Chen, T.-C., Zhou, X., Kline-Schoder, R., Sorensen, P., Cooks, R.G., Ouyang, Z.: Design of portable mass spectrometers with handheld probes: aspects of the sampling and miniature pumping systems. *J. Am. Soc. Mass Spectrom.* **26**, 240–247 (2015)
8. Cooks, R.G., Manicke, N.E., Dill, A.L., Ifa, D.R., Eberlin, L.S., Costa, A.B., Wang, H., Huang, G., Ouyang, Z.: New ionization methods and miniature mass spectrometers for biomedicine: DESI imaging for cancer diagnostics and paper spray ionization for therapeutic drug monitoring. *Faraday Discuss.* **149**, 247–267 (2011)
9. Wells, J.M., Roth, M.J., Keil, A.D., Grossenbacher, J.W., Justes, D.R., Patterson, G.E., Barket Jr., D.J.: Implementation of DART and DESI ionization on a fieldable mass spectrometer. *J. Am. Soc. Mass Spectrom.* **19**, 1419–1424 (2008)
10. Gross, J.H.: *Mass spectrometry : a textbook*, 2nd edn. Springer, Berlin (2011)
11. Amsden, J.J., Gehm, M.E., Russell, Z.E., Chen, E.X., Dona, S.T.D., Wolter, S.D., Danell, R.M., Kibelka, G., Parker, C.B., Stoner, B.R., Brady, D.J., Glass, J.T.: Coded apertures in mass spectrometry. *Annu. Rev. Anal. Chem.* **10**, 141–156 (2017)
12. Chen, E.X., Russell, Z.E., Amsden, J.J., Wolter, S.D., Danell, R.M., Parker, C.B., Stoner, B.R., Gehm, M.E., Glass, J.T., Brady, D.J.: Order of magnitude signal gain in magnetic sector mass spectrometry via aperture coding. *J. Am. Soc. Mass Spectrom.* **26**, 1633–1640 (2015)
13. Russell, Z.E., Chen, E.X., Amsden, J.J., Wolter, S.D., Danell, R.M., Parker, C.B., Stoner, B.R., Gehm, M.E., Brady, D.J., Glass, J.T.: Two-dimensional aperture coding for magnetic sector mass spectrometry. *J. Am. Soc. Mass Spectrom.* **26**, 248–256 (2015)
14. Russell, Z.E., DiDona, S.T., Amsden, J.J., Parker, C.B., Kibelka, G., Gehm, M.E., Glass, J.T.: Compatibility of spatially coded apertures with a miniature Mattauch-Herzog mass spectrograph. *J. Am. Soc. Mass Spectrom.* **27**, 578–584 (2016)
15. Bleakney, W.: Focusing and separation of charged particles. US Patent US2221467 A: (1940)
16. Bleakney, W., Hipple Jr., J.A.: A new mass spectrometer with improved focusing properties. *Phys. Rev.* **53**, 521–529 (1938)
17. Mariner, T., Bleakney, W.: A large mass spectrometer employing crossed electric and magnetic fields. *Rev. Sci. Instrum.* **20**, 297–303 (1949)
18. Monk, G.W., Graves, J.D., Horton, J.L.: A 40-cm trochoidal type mass spectrometer: Trochotron. *Rev. Sci. Instrum.* **18**, 796–796 (1947)
19. Monk, G.W., Werner, G.K.: Trochotron design principles. *Rev. Sci. Instrum.* **20**, 93–96 (1949)
20. Consolidated Electrodynamics Corporation: Mass spectrometry: Out of the laboratory...into the plant. *Anal. Chem.* **28**, 15A–15A (1956). <https://pubs.acs.org/doi/10.1021/ac60112a715>
21. Robinson, C.F.: Nonuniform fields in cycloidal-focusing mass spectrometers. *Rev. Sci. Instrum.* **27**, 509 (1956)
22. Robinson, C.F.: Space charge in cycloidal-focusing mass spectrometers. *Rev. Sci. Instrum.* **27**, 512–513 (1956)
23. Robinson, C.F., Hall, L.G.: Small general purpose cycloidal-focusing mass spectrometer. *Rev. Sci. Instrum.* **27**, 504–508 (1956)
24. Varian: This is Varian's new mass spectrometer - the double-focusing M-66. *Anal. Chem.* **38**, 117A–119A (1966). <https://pubs.acs.org/doi/10.1021/ac60235a822>
25. Varian: Does a mass spectrometer have to be massive? *Anal. Chem.* **38**, 14A–14A (1966). <https://pubs.acs.org/doi/10.1021/ac60239a711>
26. Varian Analytical Instrument Division: Mass spectrometry at work No. 4: Accurate mass measurement. *Anal. Chem.* **39**, 53A–53A (1967). <https://pubs.acs.org/doi/10.1021/ac60252a746>

27. Benz, H., Brown, H.W.: Observation of metastable ions in a cycloidal mass spectrometer. *J. Chem. Phys.* **48**, 4308–4310 (1968)
28. Schram, B.L., Adamczyk, B., Boerboom, A.J.H.: A cycloidal mass spectrometer with 100% collection efficiency. *J. Sci. Instrum.* **43**, 638 (1966)
29. Adamczyk, B., Bederski, K., Wójcik, L.: Mass spectrometric investigation of dissociative ionization of toxic gases by electrons at 20–1000 eV. *Biol. Mass Spectrom.* **16**, 415–417 (1988)
30. Adams, N.G., Smith, D.: A multicollector, cycloidal focusing, magnetic mass spectrometer. *J. Phys. E.* **7**, 759 (1974)
31. Smith, D., Adams, N.G.: An improved detector for a multicollector, cycloidal focusing, magnetic mass spectrometer. *J. Phys. E.* **8**, 44 (1975)
32. Halas, S.: Dual collector cycloidal mass spectrometer for precision analysis of hydrogen isotopes. *Int. J. Appl. Radiat. Isot.* **36**, 957–960 (1985)
33. Hemond, H.F.: A backpack-portable mass spectrometer for measurement of volatile compounds in the environment. *Rev. Sci. Instrum.* **62**, 1420–1425 (1991)
34. Hemond, H., Camilli, R.: NEREUS: Engineering concept for an underwater mass spectrometer. *TrAC Trend Anal. Chem.* **21**, 526–533 (2002)
35. Camilli, R., Hemond, H.F.: NEREUS/Kemonaut, a mobile autonomous underwater mass spectrometer. *TrAC Trend Anal. Chem.* **23**, 307–313 (2004)
36. Camilli, R., Duryea, A.N.: Characterizing spatial and temporal variability of dissolved gases in aquatic environments with in situ mass spectrometry. *Environ. Sci. Technol.* **43**, 5014–5021 (2009)
37. Blase, R.C., Miller, G., Westlake, J., Brockwell, T., Ostrom, N., Ostrom, P.H., Waite, J.H.: A compact $E \times B$ filter: a multi-collector cycloidal focusing mass spectrometer. *Rev. Sci. Instrum.* **86**, 105105 (2015)
38. Milne, W.I., Teo, K.B.K., Amaratunga, G.A.J., Legagneux, P., Gangloff, L., Schnell, J.P., Semet, V., Thien Binh, V., Groening, O.: Carbon nanotubes as field emission sources. *J. Mater. Chem.* **14**, 933–943 (2004)
39. Radauscher, E.J., Keil, A.D., Wells, M., Amsden, J.J., Piascik, J.R., Parker, C.B., Stoner, B.R., Glass, J.T.: Chemical ionization mass spectrometry using carbon nanotube field emission electron sources. *J. Am. Soc. Mass Spectrom.* **26**, 1903–1910 (2015)
40. Evans-Nguyen, T., Parker, C.B., Hammock, C., Monica, A.H., Adams, E., Becker, L., Glass, J.T., Cotter, R.J.: Carbon nanotube electron ionization source for portable mass spectrometry. *Anal. Chem.* **83**, 6527–6531 (2011)
41. Liang-Yu, C., Velasquez-Garcia, L.F., Xiazhi, W., Teo, K., Akinwande, A.I.: A microionizer for portable mass spectrometers using double-gated isolated vertically aligned carbon nanofiber arrays. *Electron Devices IEEE Trans.* **58**, 2149–2158 (2011)
42. Velasquez-Garcia, L.F., Gassend, B.L.P., Akinwande, A.I.: CNT-based MEMS/NEMS gas ionizers for portable mass spectrometry applications. *J. Microelectromech. Syst.* **19**, 484–493 (2010)
43. Tassetti, C.-M., Mahieu, R., Danel, J.-S., Peyssonneaux, O., Progent, F., Polizzi, J.-P., Machuron-Mandard, X., Duraffourg, L.: A MEMS electron impact ion source integrated in a microtime-of-flight mass spectrometer. *Sensors Actuators B Chem.* **189**, 173–178 (2013)
44. Grzebyk, T., Gorecka-Drzazga, A., Dziuban, J.A.: MEMS-type self-packaged field-emission electron source. *Electron Devices IEEE Trans.* **62**, 2339–2345 (2015)
45. Bower, C.A., Gilchrist, K.H., Piascik, J.R., Stoner, B.R., Natarajan, S., Parker, C.B., Wolter, S.D., Glass, J.T.: On-chip electron-impact ion source using carbon nanotube field emitters. *Appl. Phys. Lett.* **90**, 124102 (2007)
46. Natarajan, S., Parker, C.B., Piascik, J.R., Gilchrist, K.H., Stoner, B.R., Glass, J.T.: Analysis of 3-panel and 4-panel microscale ionization sources. *J. Appl. Phys.* **107**, 124508 (2010)
47. Radauscher, E.J., Parker, C.B., Gilchrist, K.H., Di Dona, S., Russell, Z.E., Hall, S.D., Carlson, J.B., Grego, S., Edwards, S.J., Sperline, R.P., Denton, M.B., Stoner, B.R., Glass, J.T., Amsden, J.J.: A miniature electron ionization source fabricated using microelectromechanical systems (MEMS) with integrated carbon nanotube (CNT) field emission cathodes and low-temperature co-fired ceramics (LTCC). *Int. J. Mass Spectrom.* (2016). <https://doi.org/10.1016/j.ijms.2016.10.021>
48. Harwit, M., Sloane, N.J.A.: Hadamard transform optics. Academic Press, New York (1979)
49. Landry, D.M.W., Kim, W., Amsden, J.J., DiDona, S.T., Choi, H., Haley, L., Russell, Z.E., Parker, C.B., Glass, J.T., Gehm, M.E.: Effects of magnetic and electric field uniformity on coded aperture imaging quality in a cycloidal mass analyzer. In preparation
50. Felton, J.A., Schilling, G.D., Ray, S.J., Sperline, R.P., Denton, M.B., Barinaga, C.J., Koppelaar, D.W., Hieftje, G.M.: Evaluation of a fourth-generation focal plane camera for use in plasma-source mass spectrometry. *J. Anal. Atom. Spectrom.* **26**, 300–304 (2011)
51. Chemistry WebBook, NIST standard reference database number 69. Linstrom, P.J., Mallard, W.G. (Eds.) National Institute of Standards and Technology: Gaithersburg, MD (2016)
52. Lucy, L.B.: An iterative technique for the rectification of observed distributions. *Astron. J.* **79**, 745 (1974)
53. Richardson, W.H.: Bayesian-based iterative method of image restoration. *J. Opt. Soc. Am.* **62**, 55–59 (1972)